Geomagnetic Storm Effects on the LEO Proton Flux During Solar Energetic Particle Events

Girgis, Kirolosse M.
International Research Center for Space and Planetary Environmental Science (i-SPES) Kyushu University, ■Aerospace Engineering Department Faculty of Engineering, Cairo University

Hada, Tohru
International Research Center for Space and Planetary Environmental Science (i-SPES) Kyushu University, ■Department of Advanced Environmental Science and Engineering Faculty of Engineering Sciences, Kyushu University

Yoshikawa, Akimasa
International Research Center for Space and Planetary Environmental Science (i-SPES) Kyushu University, ■Department of Earth and Planetary Sciences Graduate School of Sciences, Kyushu University

Matsukiyo, Shuichi
International Research Center for Space and Planetary Environmental Science (i-SPES) Kyushu University, ■Department of Advanced Environmental Science and Engineering Faculty of Engineering Sciences, Kyushu University

他

https://hdl.handle.net/2324/7330310

出版情報：Space Weather. 21 (12), 2023-12. American Geophysical Union (AGU)
バージョン：

AGU ADVANCING EARTH AND SPACE SCIENCES

Space Weather®

RESEARCH ARTICLE

10.1029/2023SW003664

Geomagnetic Storm Effects on the LEO Proton Flux During Solar Energetic Particle Events

Kirolosse M. Girgis[1,2], Tohru Hada[1,3], Akimasa Yoshikawa[1,4], Shuichi Matsukiyo[1,3], Viviane Pierrard[5,6], and Susan W. Samwel[7]

[1]International Research Center for Space and Planetary Environmental Science (i-SPES), Kyushu University, Fukuoka, Japan, [2]Aerospace Engineering Department, Faculty of Engineering, Cairo University, Giza, Egypt, [3]Department of Advanced Environmental Science and Engineering, Faculty of Engineering Sciences, Kyushu University, Kasuga, Japan, [4]Department of Earth and Planetary Sciences, Graduate School of Sciences, Kyushu University, Fukuoka, Japan, [5]Royal Belgian Institute for Space Aeronomy, Solar-Terrestrial Centre of Excellence, Brussels, Belgium, [6]Center for Space Radiations (CSR) and Georges Lemaître Centre for Earth and Climate Research (TECLIM), Earth and Life Institute (ELI), Université Catholique de Louvain (UCLouvain), Louvain-La-Neuve, Belgium, [7]National Research Institute of Astronomy and Geophysics (NRIAG), Helwan, Egypt

Key Points:

- We have numerically modeled the Low-Earth Orbit proton flux due to precipitated solar protons for different geomagnetic storm conditions
- Our test particle simulations reproduced the proton flux enhancement at high latitudes, agreeing with observations and cutoff rigidities
- During a stronger geomagnetic storm and solar energetic particle event, a spacecraft that enters the polar cap region would be subject to more radiation risks

Correspondence to:

K. M. Girgis,
girgiskirolosse@esst.kyushu-u.ac.jp

Citation:

Girgis, K. M., Hada, T., Yoshikawa, A., Matsukiyo, S., Pierrard, V., & Samwel, S. W. (2023). Geomagnetic storm effects on the LEO proton flux during solar energetic particle events. *Space Weather*, *21*, e2023SW003664. https://doi.org/10.1029/2023SW003664

Received 1 AUG 2023
Accepted 27 NOV 2023

Abstract

During a few solar energetic particle (SEP) events, solar protons were trapped within the geomagnetic field and reached the outer edge of the inner radiation belt. We reproduced this phenomenon by modeling the proton flux distribution at the Low-Earth Orbit (LEO) for different geomagnetic conditions during solar particle events. We developed a three-dimensional relativistic test particle simulation code to compute the 70–180 MeV solar proton Lorentz trajectories in low L-shell range from 1 to 3. The Tsyganenko model (T01) generated the background static magnetic field with the IGRF (v12) model. We have selected three Dst index values: −7, −150, and −210 nT, to define quiet time, strong, and severe geomagnetic storms and to generate the corresponding inner magnetic field configurations. Our results showed that the simulated solar proton flux was more enhanced in the high-latitude regions and more expanded toward the lower latitude range as long as the geomagnetic storm was intensified. Satellite observations and geomagnetic cutoff rigidities confirmed the numerical results. Furthermore, the LEO proton flux distribution was deformed, so the structure of the proton flux inside the South Atlantic Anomaly (SAA) became longitudinally extended as the Dst index decreased. Moreover, we have assessed the corresponding radiation environment of the LEO mission. We realized that, for a higher inclined LEO mission during an intense geomagnetic storm ($Dst = -210$ nT), the probability of the occurrence of the Single Event Upset (SEU) rates increased by 19% and the estimated accumulated absorbed radiation doses increased by 17% in comparison with quiet conditions.

Plain Language Summary

Solar energetic particles are high-energy particles emitted from the Sun during intense activity. When they reach the Earth, they become trapped in its magnetic field. In some cases, these trapped solar particles can penetrate deeper toward the Earth's surface when some fluctuations in the Earth's magnetic field occur. The impact of solar particles on satellite technologies and astronauts is significant and dangerous. In this work, we reproduced this phenomenon by developing a numerical code to calculate the solar proton trajectories inside the Earth's magnetic field according to several geomagnetic conditions. Our new results successfully produced the same physical process and did agree with other methodologies, such as satellite observations. Afterward, we estimated the resulting radiation environment of a Low-Earth Orbit mission. We found that a satellite could suffer more radiation risks of around 20% if a Solar Energetic Particle event occurred during an intense geomagnetic storm.

1. Introduction

The average lifetime of a Low-Earth Orbit (LEO) mission is from 7 to 10 years (Borthomieu, 2014). Space mission design requires a thorough process to guarantee its vital instruments' reliability and performance during a varying space environment. The LEO space missions are regularly subject to radiation risks when passing through the inner trapped radiation belt populated by energetic particles.

Energetic particles harm LEO missions and put them into dreadful situations. They can penetrate spacecraft's shielding and destroy living cells and electronic devices. Factors in assessing the resulting hazards include the composition and thickness of the shielding and the element composition of the colliding particles. Solar protons with an energy of 10–100 MeV are especially dangerous.

During their lifetime, satellites in low-altitude polar orbits accumulate radiation doses several times higher than the designed limits, disrupting computer memory chips and circuits. During their lifetime, satellites in low-altitude polar orbits accumulate radiation doses several times higher than the lethal human limit with results ranging from damaged surface materials to logic circuit upsets in computer memories and control mechanism. Because the SEP events are still unpredictable, the only strategies for mitigation are thicker shielding, careful selection of materials, and the continuous testing of the electric/electronic systems. High-energy particles are shielded from low latitudes by the Earth's magnetic field. However, they can access the ionosphere in the polar caps where magnetic field shielding is not sufficiently effective (Suess & Tsurutani, 1998).

Our planet possesses a unique magnetic field configuration due to its high-order non-dipole terms, which create non-homogeneous regions of low and large magnetic field intensities. The most particular region is the South Atlantic Anomaly (SAA), the location of the weakest magnetic field. Therefore, the inner radiation belt particles move closer to the Earth's surface and create an adverse effect: a localized region of high particle fluxes. In turn, radiation doses and Single Event Effects (SEE) considerably increase and disturb the smooth operations of the space mission instruments, occasionally leading to their failure. As space weather is driven essentially by solar conditions, thus, the inner magnetosphere and the radiation belts are consequently influencing the LEO environment.

Extensive efforts have been devoted to understanding the anomaly variations to external space weather conditions. For instance, the magnetic field variations of the SAA have been investigated for solar wind conditions using the combined IGRF and Tsyganenko models (K. M. Girgis & Hada, 2018; K. M. Girgis et al., 2020a, 2020b; Qin et al., 2014). Moreover, several observations and numerical models have been carried out to understand the inner radiation belt and the SAA's relationship with solar activity and geomagnetic conditions (Dachev, 2018; K. M. Girgis et al., 2020a, 2020b; K. M. Girgis, Hada, & Matsukiyo, 2022; K. M. Girgis, Hada, Matsukiyo, & Yoshikawa, 2021; Selesnick et al., 2010; Zou et al., 2011, 2015). Furthermore, several works assessed the resulting radiation environment on LEO space missions (Dachev et al., 2017; Falguere et al., 2002; K. M. Girgis, Hada, & Matsukiyo, 2021; K. M. Girgis, Hada, Matsukiyo, & Yoshikawa, 2022).

However, the SAA is not the only danger zone for the LEO missions; the high-latitude regions are also exposed to large particle flux in SEP events, especially during geomagnetic storms. Figure 1.5 from the textbook of National Research Council (2000) displays a schematic representation showing qualitatively the approximate limits of the small and large exposed areas of the two high-latitude particle flux bands during quiet and geomagnetic storm conditions respectively, when a SEP event occurs.

1.1. Evidence From Observations

Various observations demonstrated the solar proton precipitation with great detail, for example, (Falguere et al., 2002; Qin et al., 2014). However, few observations showed that the incoming solar protons could penetrate in the outer boundary of the inner radiation belt at low L-shells, as found by Slocum et al. (2002). For instance, Pierrard et al. (2014) observed the remaining trapped solar protons around the whole month of June 2013 between $L = 4$–5 after the intense SEP event in May 2013. More recently, the large SEP event of September 2017 was investigated by Pierrard et al. (2023), who confirmed that solar protons could reach the inner belt but were immediately lost due to the following magnetic storm.

Furthermore, an important parameter related to the incoming solar protons is the geomagnetic cutoff rigidity, allowing the solar protons to access the trapping region. Leske et al. (2001) showed that the quiet time cutoffs for 20 MeV protons at $L = 4$ were near 60° invariant latitude, but lowered in correlation with the *Dst* index.

1.2. Remark About the Semi-Empirical Model AP8

Besides satellite measurements, the long-standing trapped model AP8 has proven its popularity and success for the LEO space mission design. However, the AP8 model needs to fairly represent the high-latitude proton distribution, particularly during the SEP events and magnetic storms, as well as the short-term variations of the

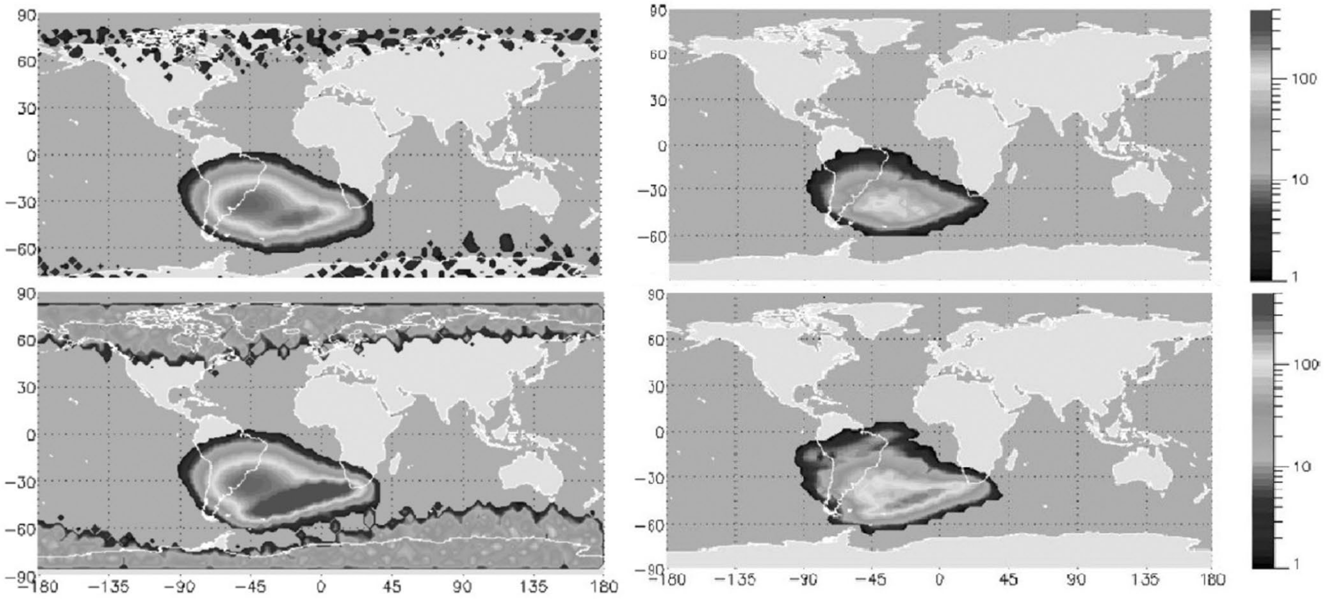

Figure 1. (Left Panel) 9.4 MeV proton fluxes maps predicted by AP8-MAX (top) and AP8-MIN (bottom). (Right Panel) 10 MeV proton flux maps measured by the ICARE instrument before (top) and after (bottom) the 31 March 2001 event (MeV^{-1} cm^{-2} s^{-1}) (Falguere et al., 2002).

inner radiation belt (E. Petersen, 2011). Figure 1 shows the mappings for the 9.4 MeV proton fluxes predicted by AP8-MAX (the upper panel) and AP8-MIN (the lower panel) (Falguere et al., 2002).

1.3. Recent Advances From Numerical Simulations

For instance, Hudson et al. (1997) simulated the solar proton injection in the low *L*-shells during the Storm Sudden Commencement (SSC). Furthermore, Kress et al. (2005) computed the solar particle Lorentz trajectories in a time-dependent perturbed dipole magnetic field from a Lyon-Feder-Mobarry (LFM) global MHD magnetospheric model simulation. In addition, Kress et al. (2010) calculated the particle cutoff rigidities during the 29–31 October 2003 geomagnetic storm by using a more realistic magnetic field represented by the Tsyganenko model (TS05) (Tsyganenko & Sitnov, 2005). Moreover, Mertens et al. (2010) applied the previous cutoff rigidity model to predict the harmful radiation exposure levels at commercial airline altitudes.

1.4. Statistical Relationship Between SEP and Geomagnetic Storms

Several works statistically investigated the connection between the SEP events and the geomagnetic storm occurrences, for example, (Selesnick et al., 2010).

We have analyzed the 266 SEP event list compiled by the NOAA Space Environment Services Center and available online https://umbra.nascom.nasa.gov/SEP/ from 1978 to 2017 and checked the SEP events manually from GOES spacecraft from 2017 to 2020. As shown in Figure 2, 75% of the SEP events were associated with the geomagnetic storms of $Dst \leq 50$ nT. This result confirms the conclusion of Ameri and Valtonen (2019) that 68% of 95 SEP events were related to geomagnetic storms with $Dst \leq 50$ nT. The previous authors used mainly the proton measurements of the Energetic and Relativistic Nuclei and Electron experiment (ERNE) aboard the Solar and Heliospheric Observatory (SOHO) from 1996 to 2017 to forecast the geomagnetic storm occurrences. Most importantly, our statistical results revealed that 51% of the detected SEP events coincided with the main and/or recovery phases of magnetic storms with Dst below −50 nT. The previous information formulates our primary motivation to carry on this research, which highlights the necessity of considering the varying space environment during active geomagnetic conditions for the shielding and circuit designs of future LEO space missions.

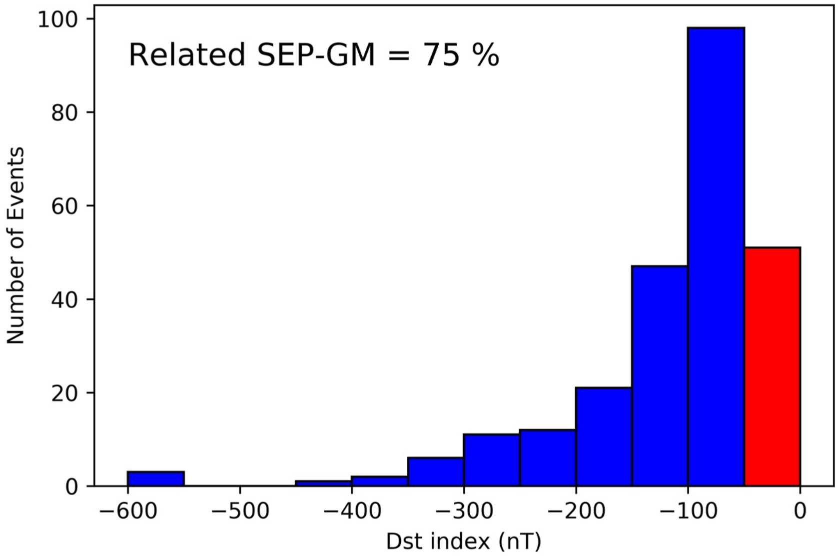

Figure 2. A statistical study relating the SEP and geomagnetic storm events from 1978 to 2020, where 75% of the SEP events were associated with the geomagnetic storms of $Dst \leq -50$ nT.

1.5. Motivation and Objective

In order to reproduce the phenomenon of the accessibility of the solar protons in lower latitudes during magnetic storms, to overcome the limitations of the semi-empirical models, and to predict the radiation environment for the LEO missions more accurately, we have performed numerical simulations of the solar proton precipitation in the inner radiation belt.

In the present work, we have conceived a new methodology with the following advantages:

1. The simulation of the solar proton trajectories in the inner radiation belt region ($1 < L < 3$) during several geomagnetic storm conditions,
2. The implementation of the very efficient integrator for particle energy conservation, the Boris-Buneman algorithm,
3. The reproduction of the proton flux distribution maps at any LEO altitude,
4. The detection of the proton flux variations at all latitudes, including both high- and low-latitude regions (SAA), and,
5. The capability to assess and predict the resulting Single Event Upset (SEU) rates and the absorbed radiation doses for a LEO spacecraft mission.

This work is considered a complementary design phase of the previous efforts of Samwel and Hady (2009) for predicting the radiation environment of EGYPTSAT-2. We present this valuable work to evaluate the particle and radiation environments of the upcoming space missions more accurately.

2. Material and Methods

2.1. Targeted Scenario

Our target was to reproduce the scenario of the solar proton trapping at the outer boundary of the inner radiation belt during a geomagnetic storm. As shown in the explanatory Figure 3, the expected output results at a selected altitude projected in a geographical map should include three hazardous regions of proton flux located in the SAA (blue), and the northern/southern latitude bands (red), respectively.

As the higher energy protons trapped in the inner belt can have a more significant radiation impact on space technology, the selected range of proton energy was from 70 to 180 MeV. Figure 4 illustrates the SEP spectrum of the worst-case scenario developed by Xapsos et al. (1999, 2000), and the inner proton belt spectrum computed

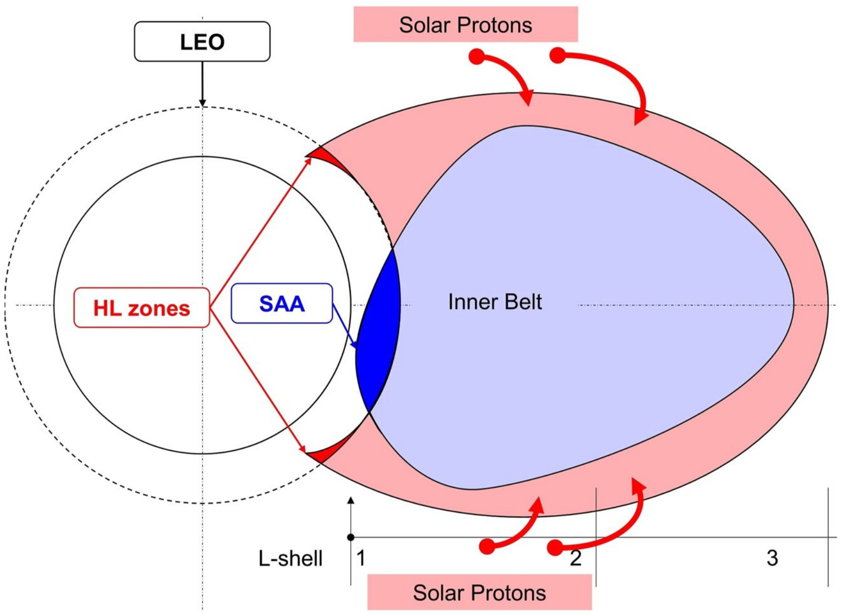

Figure 3. This schematic diagram denotes the contribution of the inner radiation belt and the trapped solar protons in its outer boundary. During a SEP event in an intense magnetic storm, the solar protons could cross the LEO trajectory and create a pair of northern and southern high-latitudinal (HL) proton bands, shown as two additional red triangular regions (K. Girgis et al., 2022).

by AP8 model (de Soria-Santacruz Pich et al., 2017). The output figure looks similar to the one published by Wilson (1978).

The inner radiation belt extends from 1 to 3 Re. Figure 5 displays the geographical projection of the guiding center particle trajectory for different *L*-shells. The trapped solar proton at the outer edge of the inner belt can reach a maximum latitude of 60°.

2.2. Quasi-Trapped Particle Simulation Model

We solved the equations of full particle motion for 10^5 protons, distributed in *L*-shells from 1 to 3, and randomly assigned an energy range from 70 to 180 MeV and a pitch angle range from 0° to 180°, as follows:

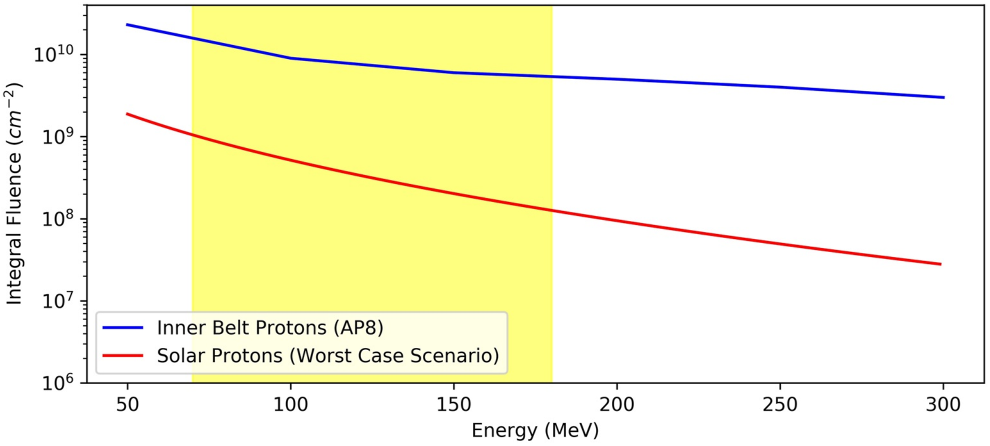

Figure 4. The figure shows the Solar Proton Event spectrum (worst-case scenario) superposed by the inner proton belt spectrum (AP8) for one active solar year. The yellow-highlighted area corresponds to the implemented proton energy in our simulations.

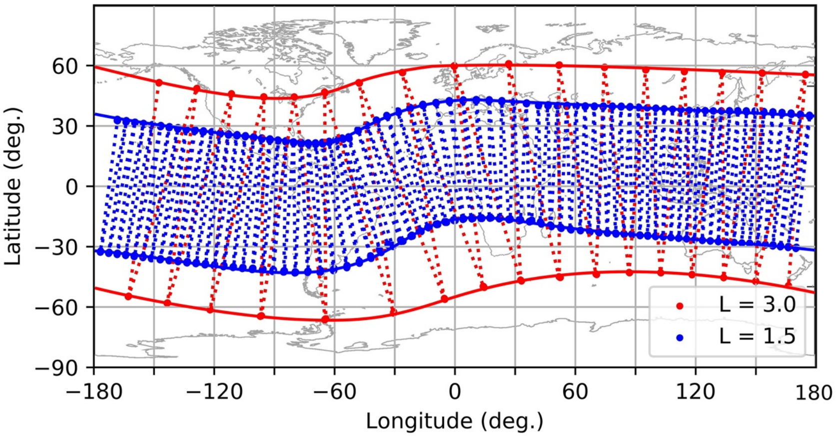

Figure 5. The figure shows the geographical footprints of the computed 1.5 and 3 L-shells by guiding center particle trajectory tracing.

$$\frac{d\mathbf{u}}{dt} = \frac{q}{m}\left(\frac{\mathbf{u}}{\gamma} \times \mathbf{B}\right) \quad (1)$$

$$\frac{d\mathbf{r}}{dt} = \frac{\mathbf{u}}{\gamma} \quad (2)$$

where $\mathbf{u} = \gamma\mathbf{v}$, $\mathbf{v}$ is the particle velocity, $\gamma = \left(1 + u^2/c^2\right)^{1/2}$ is the Lorentz factor, m is the particle rest mass, c is the speed of light, q is the particle charge, $\mathbf{B}$ is the magnetic field, and $\mathbf{r}$ is the particle position. In the simulations, proton positions and velocities were normalized by taking the length and velocity scales of the Earth's radius and light speed, respectively.

The background static geomagnetic field consisted of the IGRF-12 (Thébault et al., 2015) and Tsyganenko model T01 (Tsyganenko, 2002). According to K. M. Girgis et al. (2020a, 2020b), we have selected the Tsyganenko model T01 because it highlighted the *Dst* index effect on the geomagnetic variations at low altitudes. Considering that we focused on the proton flux distribution in the LEO due to the geomagnetic field configuration, we did not include the electric field in the current simulations for the following reasons: First, the magnetic field is the dominant factor characterizing the inner radiation belt region. On the other hand, the inductive electric field has a weak impact on the trajectories of the protons with high energy (70–180 MeV) in the low *L*-shells (K. M. Girgis et al., 2020a, 2020b). Moreover, our simulations focused on the particle dynamics in the trapping inner belt region during the geomagnetic storm. Therefore, we did not include the inductive electric field generated during the Storm Sudden Commencement (SSC) as simulated by Hudson et al. (1997). Following the argument of Kress et al. (2010), since the SEP rarely occurs during a SSC, it is reasonable to ignore the electric field and to include the effective magnetic field based on the active storm time ($Dst < -50$ nT or $Kp > 4$) because the interaction of the SEPs with the magnetosphere is on time scales shorter compared to the magnetospheric dynamics.

The system of Equations 2 was solved by the Boris-Buneman algorithm, which is known for its great energy conservation performance compared with other integrators such as the classical Runge-Kutta fourth order. This method is second order and has been specifically developed for charged particle motion because it adds additional accuracy to the magnetic gyration term, which produces the largest numerical error, and decouples the magnetic field effect from the electric field effect (Mao & Wirz, 2011). Several authors applied this algorithm in particle simulations, such as Engel et al. (2015) and K. M. Girgis, Hada, and Matsukiyo (2022). The more detailed explanation of the algorithm implementation is found in Appendix A.

As it was extremely time-consuming to compute the magnetic field at all particle positions at each time step, we introduced a grid to the system. We used linear interpolation to find the magnetic field at any given location. The entire magnetic field grid system was a cube with dimensions of 6 Re × 6 Re × 6 Re, its grid space size resolution was 0.075Re, and the Earth was in the grid center.

Table 1

The Contribution of the High-Latitude Proton Flux With Respect to the Entire Proton Flux at 650 km: the Fluence (Φ) and the Time (τ) Spent in the Low- and High-Latitudinal (LL & HL) Regions

	$\Phi_{p@HL}/(\Phi_{p@HL}+\Phi_{p@LL})$	$\tau_{@HL}/\tau_{@LL}$
NPLEO	39%	66%
PLEO	36%	80%

To initially distribute the protons uniformly in all L shells, we followed the same procedure of Saito et al. (2010). We calculated the drift period of one single proton in the implemented magnetic field. Afterward, we multiplied the calculated drift period of the single proton by a uniform random number from 0 to 1 to obtain the drift period of every proton.

We performed three simulations according to three geomagnetic field configurations defined by three Dst index values: −7, −150, and −210 nT, denoting quiet, strong, and intense magnetic storms with keeping the rest of the solar wind inputs unchanged.

We stopped each run when protons with the lowest energy performed about six drifts, corresponding to approximately 1 min in real-time. The protons were collected below $1.15R_e$. Then, the proton positions were converted from Cartesian to geodetic coordinates: height, latitude, and longitude. In the next step, the fluxes were calculated by a three-dimensional interpolation: height, latitude, and longitude. The mapped grid resolution at any desired altitude was $1.0° \times 1.0°$.

In the current study, we considered the proton fluxes directional integral fluxes, where the protons pass inward through a unit area of degree^2 of the geographical map in 1 s for a 2π solid angle and for all energy ranges. Thus, the corresponding flux unit would be deg^{-2} s^{-1} str^{-1}.

2.3. Radiation Analysis

We have implemented the same methodology as applied by K. M. Girgis, Hada, and Matsukiyo (2021) and K. M. Girgis, Hada, Matsukiyo, and Yoshikawa (2022) to calculate both radiation parameters: the Single Event Upset (SEU) rates and the absorbed radiation doses.

2.3.1. SEU Rates

The Single Event Upsets (SEUs) due to protons introduce severe problems in the electronic circuitry of earth-orbiting spacecraft. The SEU is a change of state caused by an ionizing particle striking a sensitive node in a microelectronic device, such as in a microprocessor, semiconductor memory, or power transistors. A nuclear reaction initiated by a proton can produce sufficient ionization for an upset. The probability of proton-induced SEUs and the dependence of the upset cross-section on proton energy can be investigated both experimentally and theoretically. We estimated the SEU rates in this work by combining the semi-empirical proton upset cross-sections with the output proton spectrum from our numerical simulations. We followed the methodology established by Bendel and Petersen (1983). The more detailed explanation of the SEU estimation procedure is found in Appendix B.

2.3.2. Absorbed Radiation Doses

The absorbed dose rate was computed by the product of the charged particle fluence rate $\dot{\Phi}$ (=flux) obtained from the numerical simulations at the range X within the shielding material by the mass stopping power (S/ρ), function in the energy of the incident charged particle (Antoni & Bourgois, 2017; Blakely et al., 1984; Burrell, 1964). The unit of absorbed radiation dose rate was rad/s. The mass stopping power was given from the "Stopping Power and Range Tables for Protons for Aluminum." The more detailed derivation of the absorbed radiation dose is found in Appendix C.

3. Results

3.1. High-Latitudinal Proton Flux Contribution During a SEP Event

First, we highlighted the importance of including the high-latitudinal (HL) proton flux when defining the space environment for a selected mission during a SEP event. We have computed the ground tracks of two LEO satellites and estimated the detected proton flux along their orbits for two different inclination angles: 51°, which represents a Near-Polar LEO (NPLEO), and 98°, a Polar LEO (PLEO), for three orbit periods at the altitude 650 km. Results shown in Table 1 were calculated during a solar proton event in quiet time (when $Dst = -7$ nT).

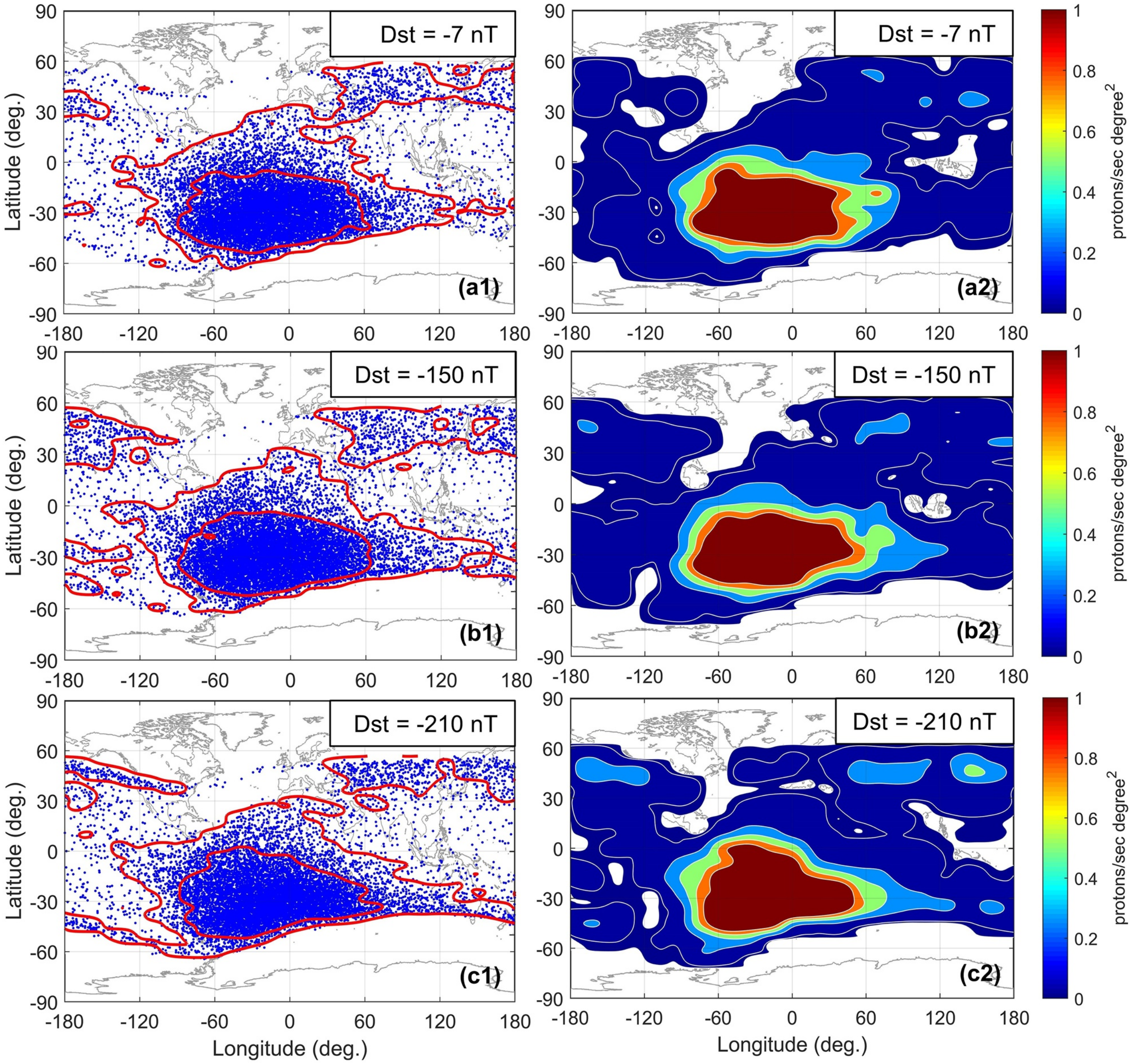

Figure 6. *Dst* index effect on the 70–180 MeV protons (Left Panels: a1, b1, and c1) and proton flux distributions (Right Panels: a2, b2, and c2) during a SEP event in the geographical map at 800 km as obtained from the numerical simulations.

Table 1 demonstrates the contribution of the HL proton flux region to the entire proton flux at 650 km. The HL fluence measured by both missions was almost similar, but their contributions were significant (above 35%) for the entire LEO fluence map. Furthermore, a PLEO spacecraft would spend more time in the HL regions than in the LL region where the SAA is located and can reach almost the same duration it could spend in the LL region (≈80%).

3.2. Proton and Proton Flux Distributions

Figure 6 illustrates the proton distribution (Panels a1, b1, and c1) and the corresponding proton flux distribution (Panels a2, b2, and c2) obtained with the simulations described in Section 2.2 on the geographical map at 800 km. Note that as long as the *Dst* index was decreased, the high-latitudinal proton flux became more prominent and moved slightly to the lower latitude range. Moreover, simulation results showed a notice-

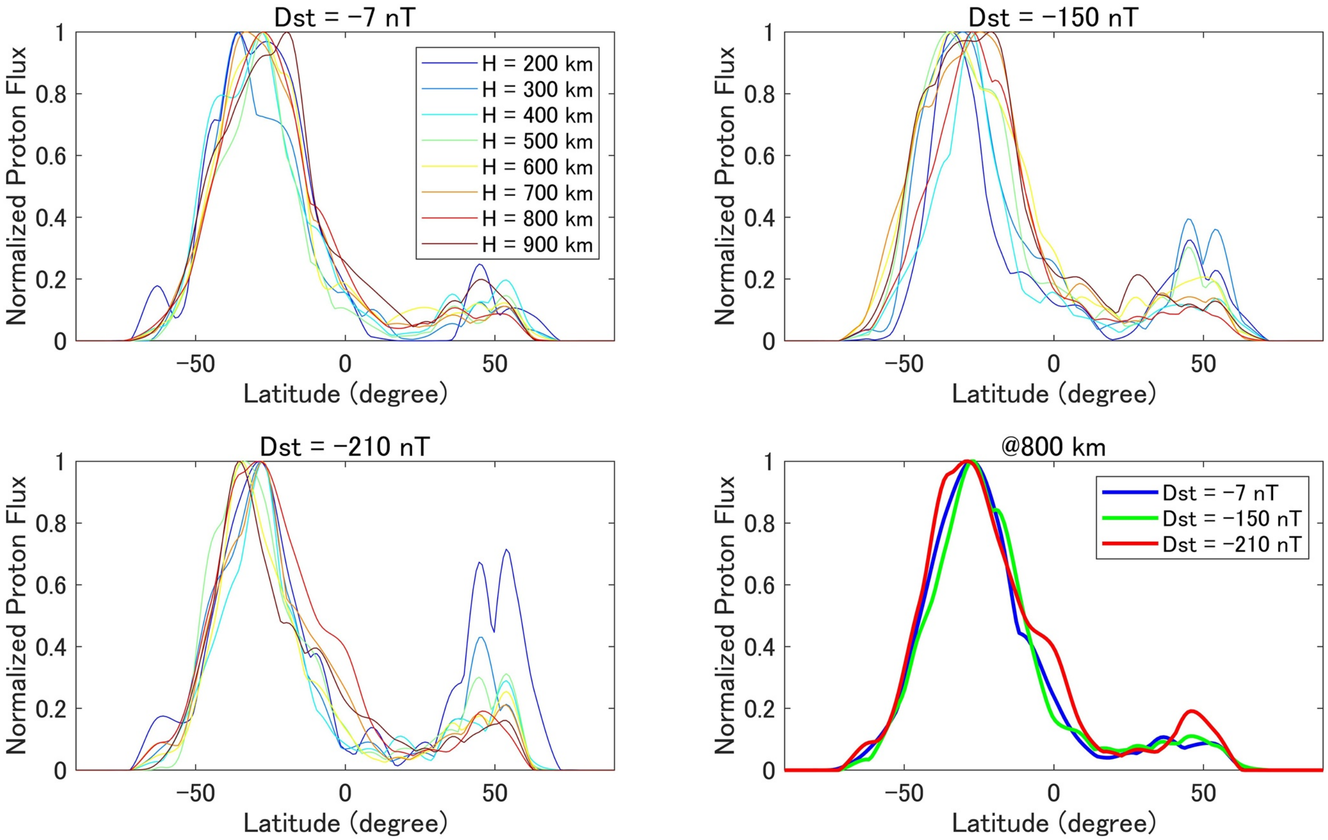

Figure 7. Longitudinal proton flux distributions at different altitudes during several geomagnetic conditions (*Dst* index) in a SEP event. In order to smoothly quantify the variations, the vertical axis represents the normalized proton flux, computed by dividing the proton fluxes by the maximum value.

able longitudinal extension of the proton flux distribution in the SAA extension as long as the *Dst* index was decreased. This effect was evident in the SAA's southern border, which merged with the southern hemisphere's proton flux.

3.3. Altitude Effect on the Proton Flux Distribution

One of the merits of performing numerical simulations is the reproduction of the proton flux maps at any desired altitude. Figure 7 shows the longitudinal proton flux at altitudes from 200 to 900 km. Latitude range [−60°, 10°] corresponds to the proton flux inside the SAA overlaid with the southern high latitude band and the range [30°, 80°] to the northern high-latitude proton flux band. We observe the enhancement of the proton flux at the high latitudinal regions of the North Hemisphere for different *Dst* indices. This enhancement was more significant at lower altitudes than at higher altitudes. For instance, at an altitude of 200 km, specifically during the intense geomagnetic storm when $Dst = -210$ nT, the increase of the high-latitudinal proton flux reached approximately 75% of the maximum SAA proton flux that we took as reference. We have selected the proton flux distribution at 800 km to elucidate the effect of the *Dst* index, as shown in the bottom right panel of Figure 7. When the *Dst* index was −210 nT, the high latitudinal proton flux growth corresponded to 20% of the maximum SAA flux.

3.4. Radiation Analysis

This section presents the more practical engineering phase, which is the effect of the HL proton flux dynamics on the radiation analysis of a LEO mission. In particular, we focused on the Polar Low-Earth Orbit (PLEO) missions since they had more access to the HL regions in addition to the SAA.

We selected the same orbit parameters of EGYPTSAT-2 as used by Samwel and Hady (2009). The orbit inclination was 98°(=PLEO mission) and the altitude was approximately 650 km. However, the spacecraft is currently

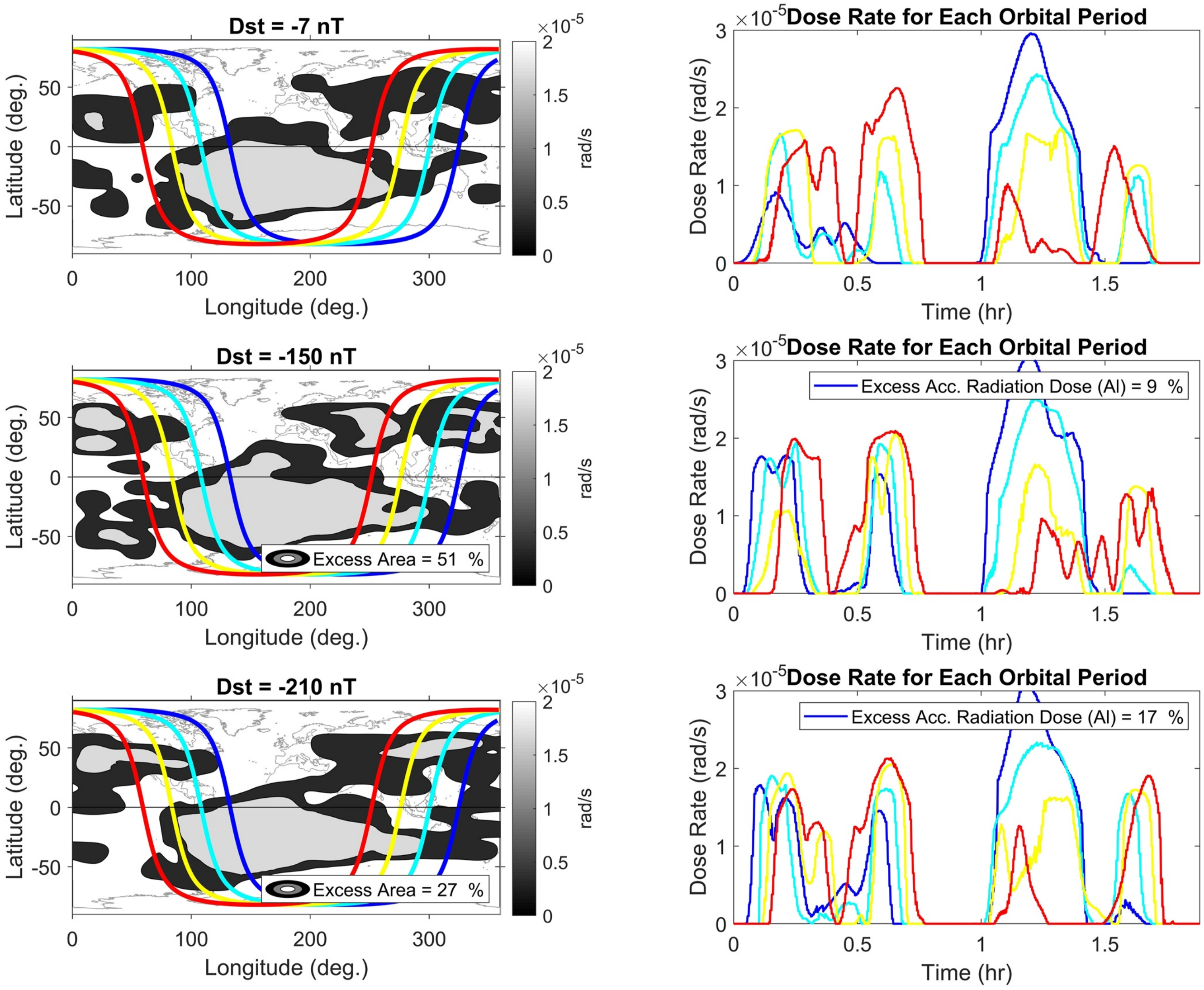

Figure 8. The left three panels represent the contour maps of the absorbed radiation dose rates overlaid by the satellite groundtracks. The three right panels show the amount of radiation doses the spacecraft would be exposed during its orbital motion at 650 km. Each groundtrack colored in the left panels corresponds to the same color of the detected dose rates displayed in the right panels.

orbiting with an inclination of 51°(=near-PLEO mission). Nevertheless, we have performed the radiation analysis for both inclination angles and compared the results, as shown in the next section.

The three left panels of Figure 8 visualize the radiation dose maps plotted with the groundtrack of the PLEO satellite. On the other hand, the three right panels display the amount of the radiation dose the spacecraft would detect when moving along its orbit. We deduced the following: (a) for the strong storm case ($Dst = -150$ nT), the higher contour levels of the radiation dose maps were more extended by 50% and the accumulated radiation dose were increased by 9% in comparison with quiet time. (b) For more intense storm case ($Dst = -210$ nT), the radiation dose boundaries were extended by 27% and the accumulated radiation dose were increased by 17% in comparison with quiet time.

Similarly, Figure 9 illustrates the predicted SEU maps for a 110 MeV incident proton energy and occurring at thickness 1 g/cm^2 for an Aluminum shielding. We deduce the following: (a) for the strong geomagnetic storm case, the SEU boundaries (= the high SEU risk level in red dots) were extended by 12% relative to the quiet time and the SEU occurrences increased by 12%. (b) For more intense storm case, the radiation dose boundaries were extended by 18% and the accumulated radiation dose was increased by 19% in comparison with quiet time.

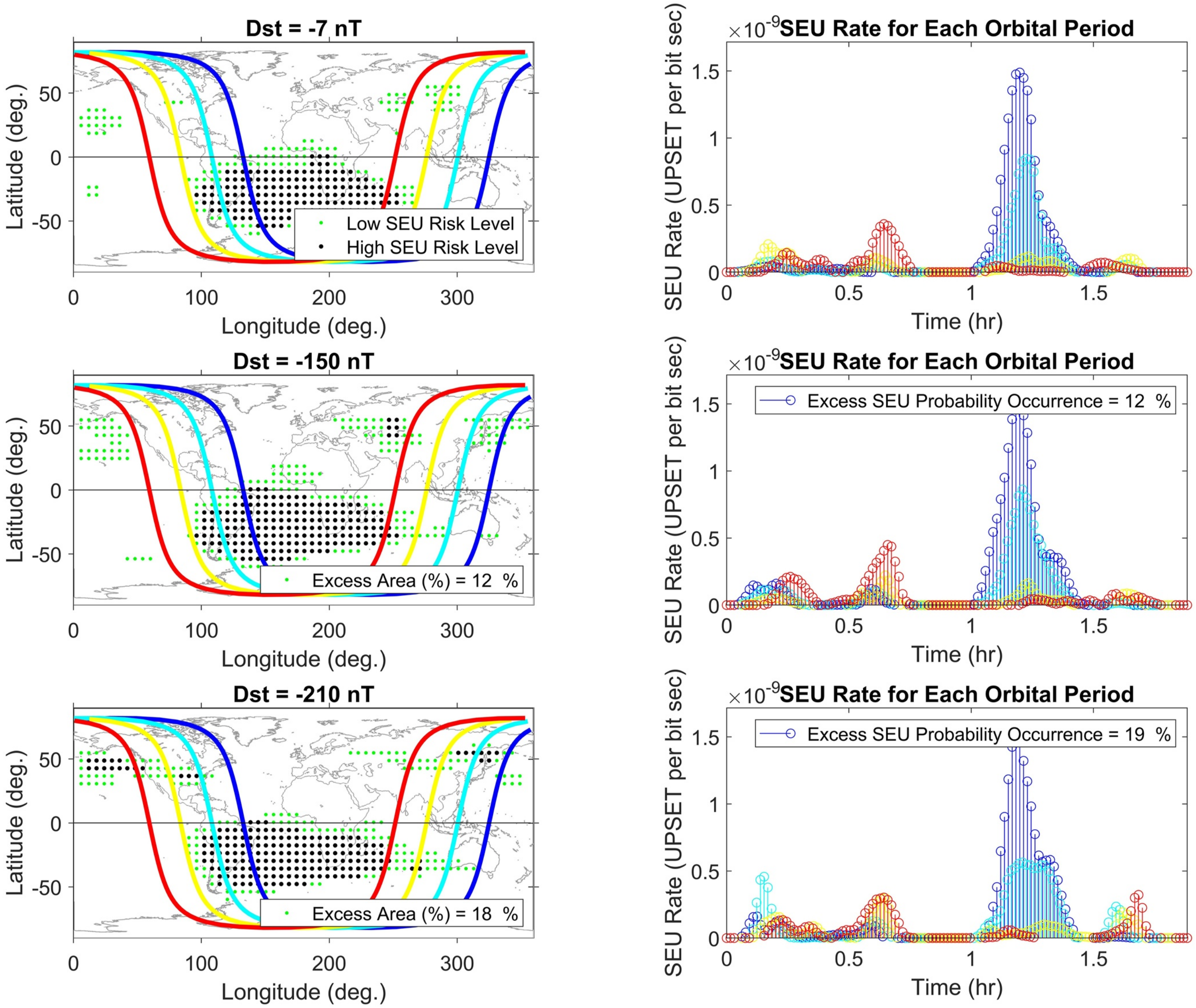

Figure 9. The left three panels represent the occurrence maps of the SEU rates overlaid by the satellite groundtracks. The three right panels show the amount of SEU the spacecraft was exposed during its orbital motion at 650 km. Each groundtrack colored in the left panels corresponds to the same color of the detected SEU rates displayed in the right panels.

Table 2
Radiation Analysis for Two Different Polar Orbit Space Missions During Two Geomagnetic Storm Levels in SEP Event Showing the Excess Percentage of Both Radiation Parameters: the Accumulated Absorbed Radiation Doses and the SEU Occurrences, With Respect to Quiet Time When Dst = −7 nT

	Near-polar orbit mission		Polar orbit mission	
Dst index	Radiation doses	SEU occurrences	Radiation doses	SEU occurrences
−150 nT	+16%	+11%	+9%	+12%
−210 nT	+12%	+3%	+17%	+19%

3.5. Orbit Type Effect on the Radiation Analysis

Since the radiation analysis of a LEO orbit depends essentially on the orbit inclination, we have further assessed the radiation environment for a NPLEO ($i = 51°$). Table 2 demonstrates the excess percentage of accumulated radiation doses and SEU rates due to SEP events during geomagnetic storms relative to quiet time for both NPLEO and PLEO missions. The latter was more exposed to radiation risks than the NPLEO during a more intense magnetic storm. This was true for the NPLEO mission but during a less intense magnetic storm. The reasons were that the NPLEO mission could not fully cover the HL proton flux regions and that the SAA proton flux area was slightly deformed.

4. Discussion

4.1. The Interpretation of the Proton Flux Enhancement at the HL Regions in a SEP Event During Geomagnetic Storms

The reason behind the enhancement of the proton flux at the high-latitude regions could be explained by several methods, though the primary reason is the magnetic field configuration:

(a) In our previous work (K. M. Girgis et al., 2020a, 2020b), we demonstrated the effect of the *Dst* index on the geomagnetic field variations, including the SAA and the two magnetic poles. We found that the boundary of the low magnetic field intensity was expanding toward higher latitudinal regions which became a more favorable condition for the particles to penetrate in the high-latitude regions.
(b) Furthermore, the geomagnetic cutoff rigidities explain the accessibility of the particles in the HL regions and their extension toward the equatorial zone during magnetic storms and SEP events. By computing the particle tracing backward in time, Smart and Shea (1994) and Smart and Shea (2005) developed the geomagnetic cutoff rigidity maps. They revealed that the cutoff latitudes decreased according to the increase of the Kp index.
(c) Moreover, the latitudinal variation of the particle mirror points can interpret the mechanism of the solar proton precipitation. Lemaire et al. (2005) solved the relativistic Lorentz's equations of particle motion to prove that the latitude of the mirror points decreased when the IMF turned southward, indicating the enhancement of the ring current defined by the *Dst* index.
(d) Recently, the observations of the EPT/PROBA-V mission showed the changes of the SAA region borders in the first six months of 2015 when the trapped L-shells were reduced from 3 to 2.8 due to the SEP event occurred on 15 March 2015 (Pierrard & Rosson, 2016). In addition, the R3DR2/ISS measurements demonstrated the decrease of the outer boundary of the inner radiation belt during the magnetic storm of March 2015 from $L = 3$ to 2.3, and during April, May and partly June, from $L = 3$ to $L = 2.5$ (Dachev, 2018).

Similar to the conclusions of the research studies mentioned earlier, our simulation results revealed that during SEP events, the computed proton distribution was longitudinally more extended at the LL and more concentrated at the HL regions as the geomagnetic storm intensified. It was true that the *Dst* index indicated an enhancement in the HL proton flux but not necessarily an increase in the entire LEO proton flux, which means that the HL zones were more susceptible for magnetic and particle flux changes than the LL zones during geomagnetic storms when SEP occurred. In some cases, the HL proton flux intensity can surpass the SAA proton flux, as reported by Pierrard et al. (2014).

In addition, we reproduced the energy distribution of the flux during the storm events. Figure 10 displays the increase of the curves' steepness for more intense storms. We drew two important conclusions: the first was the loss of the higher energetic protons due to the increased field line curvature when *Dst* index decreased (Selesnick et al., 2010; Zou et al., 2011), and the second was the precipitation of the lower energetic protons during increased storm intensity.

4.2. The *Dst* Index Effect on the Radiation Analysis

The results of our radiation prediction model indicated that during a solar proton event, the two radiation parameters behave differently depending on the orbit inclination, so a NPLEO spacecraft could be subject to an acute radiation environment during a strong storm ($Dst = -150$ nT). In contrast, the acute radiations for the PLEO spacecraft case appeared more significant during an intense storm ($Dst = -210$ nT). This result implies that, since the accumulated radiation dose is time-dependent, the NPLEO spacecraft can be more exposed to higher radiation levels if the strong geomagnetic storm persists for several days. It further implies that the enhanced HL proton flux zones increase the probability of exposing the PLEO satellite to more Single Event Effects (SEE) during an intense storm. Eventually, the growth of both radiation parameters imposes a substantial threat to the satellite operation and performance.

4.3. The Possible Cause of the Loss of EGYPTSAT-2

We present here as a case study the remote sensing satellite EGYPTSAT-2: Samwel and Hady (2009) adequately carried out the radiation analysis of the mission by combining several semi-empirical models where one of them

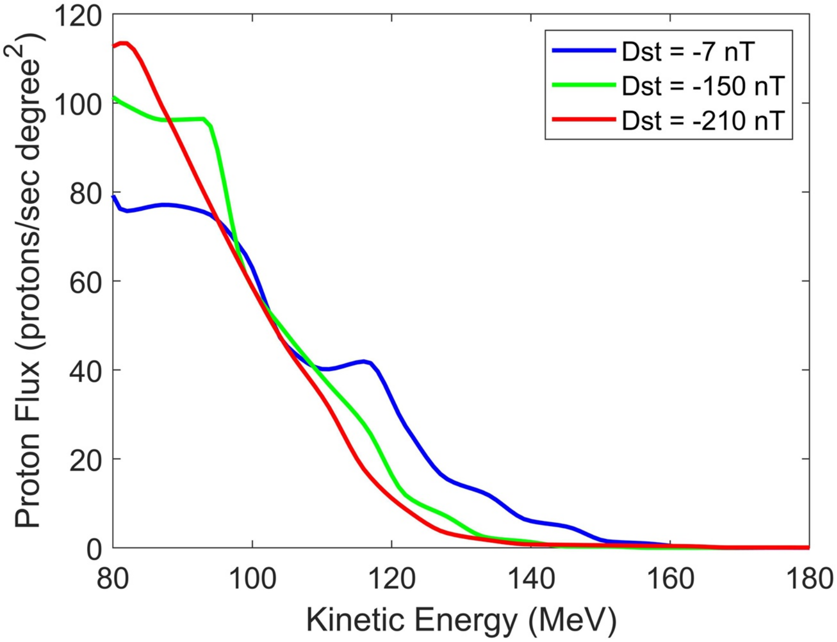

Figure 10. Proton energy spectrum reproduced from the numerical simulations for the three *Dst* conditions.

was the AP8 trapped model. Unfortunately, one year after its launch date (16 April 2014), the satellite was out of control, and the 11-year planned mission terminated unsuccessfully (https://directory.eoportal.org/web/eoportal/satellite-missions/e/egyptsat-2#overview).

According to the previous ESA eoPortal website, the remote sensing satellite EGYPTSAT-2 was out of control in June 2015 after a series of technical problems, where the last contact was in April 2015. The cause of its failure was not yet revealed.

When investigating the solar and geomagnetic conditions during the previous months before its failure, it was revealed that a SEP event had occurred on 15 March 2015. By using the EPT instrument mounted on the PROBA-V satellite, Pierrard and Rosson (2016) identified a solar flux of 8 particles cm^{-2} s^{-1} sr^{-1} for energies higher than 10 MeV (which was just below the threshold to be considered as a full SEP event). The new set of EPT/PROBA-V's observations in Figure 11 confirms the precipitation of the solar protons at the high-latitude regions. The upper panel displays the LEO protons (in particular the HL distribution) before the magnetic storm occurred on 17 March. These precipitated solar protons were quickly removed during the storm and afterward, as shown in the middle panel from 17 to 31 March. Furthermore, the lower panel visualizes the proton accumulation in the high-latitudinal regions due to a more severe SEP event, coinciding with an intense magnetic storm ($Dst = -200$ nT) during the last 10 days of June.

Originally, these magnetospheric conditions were triggered due to the emissions of one X flare with several M flares in March and two consecutive M flares during April. Figures D1–D3 summarize the solar and geomagnetic activities during March and April 2015.

Regarding the satellite environment, Dachev et al. (2017) measured the radiation effects due to the activity of the inner radiation belt and the SEP events from October 2014 to January 2016. The reported radiation measurements indicated that until June, the radiation doses of the inner radiation belt were increased by a factor of 5–10 during March and April relative to quiet time. In addition, the authors detected 11 maxima of SEP daily dose rates during this period, where one maximum (around 10 time increase relative to quiet conditions) occurred at mid-March coiciding with the weak SEP event of 15 March 2015.

Given the previous space environment conditions until June 2015, and according to our numerical LEO proton flux maps and radiation assessment, with the 2015's observations of Dachev et al. (2017) and the new ones by EPT/PROBA-V, we attempt to explain that the abnormalities of EGYPTSAT-2's operations and its loss could be due to the non-inclusion of the intense activity of the inner radiation belt in the radiation design of EGYPTSAT-2

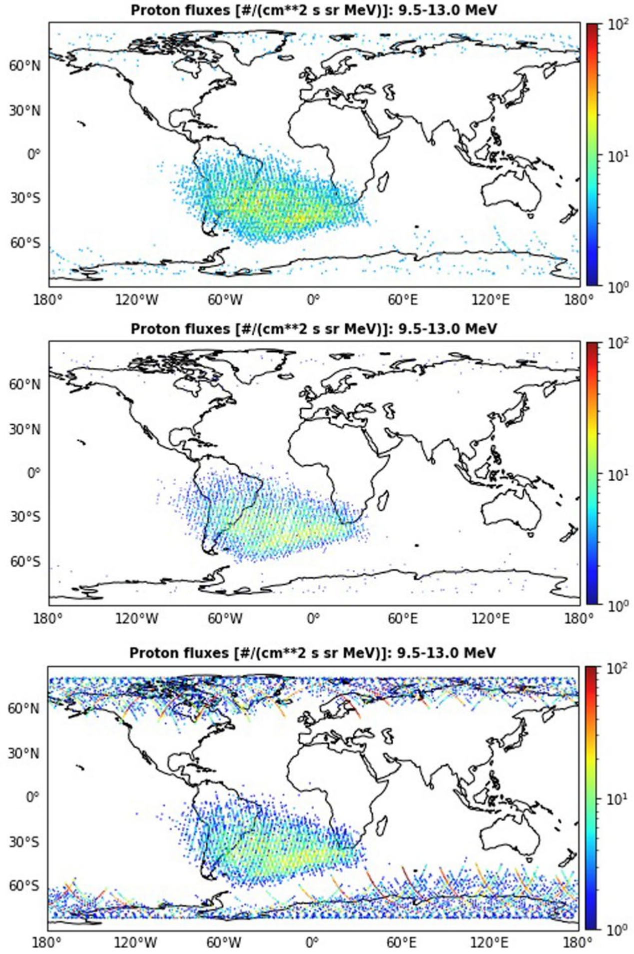

Figure 11. New observations from EPT/PROBA-V: The upper panel represents the proton flux map during 1–16 March, the middle panel during 17–31 March, and the lower panel during 20–30 June 2015.

in response to the SEP events, the geomagnetic storms, and the solar activity, which resulted in the enhancement of the HL proton flux, thus, the surge of the accumulated radiation doses and the SEU rates.

As a matter of fact, the 15–17 March 2015 event is known as the "St. Patrick's Day" event, which was widely and extensively reported by numerous works for example, the original severe solar conditions (Wu et al., 2016), the corresponding strong distortion in the high-latitude ground magnetic response (Xu et al., 2017), the resulted vertical expansion of the equatorial F-layer in the Brazilian sector (Venkatesh et al., 2017), the produced enhancement of the plasma content in the southern polar ionosphere region (Shreedevi et al., 2020), the generated steep increase in the ring current proton flux with the occurrences of ion injections (Goldstein et al., 2017), as well as the electron injections in the inner radiation belt (Dachev, 2018). The previous severe space weather conditions could be considered as additional important factors that led to the irregularities in the operations of the Egyptian satellite.

Consequently, according to the textbook of National Research Council (2000), the consideration of the high-latitudinal proton flux regions with the semi-empirical trapped models is considered a prerequisite upgrade to save future space missions from under-estimated radiation effects.

5. Conclusions and Summary

In this work, we have numerically modeled the LEO proton flux map considering the solar proton precipitation in different geomagnetic storm levels. We have developed a relativistic test particle simulation code to calculate the proton trajectories in the inner magnetosphere consisting of IGRF-12 and T01 models. Then, we have estimated the corresponding radiation environment for a satellite with two different orbit inclinations. We draw our conclusions as follows:

1. Through the implementation of numerical simulations, we showed that the incoming solar proton precipitated at high latitudes can sometimes be trapped. The resulting flux was enhanced during geomagnetic storms, as similarly detected by satellite measurements and cutoff rigidities.
2. As long as the *Dst* index was reduced, the shape of the SAA proton flux region extended longitudinally, confirming the reduction of the trapped *L*-shells as observed by satellite measurements and cutoff rigidity maps.
3. The two high-latitudinal proton flux stripes were more enhanced in lower altitudes in comparison with the SAA proton flux due to the decrease of the *Dst* index in a SEP event.
4. A lower-inclined orbit spacecraft would suffer more damage during a strong magnetic storm ($Dst = -150$ nT) than an intense one ($Dst = -210$ nT). The additional accumulated absorbed radiation doses and the excess SEU rates can reach 16% and 11%, respectively, relative to quiet conditions. On the other hand, a higher-inclined orbit spacecraft would experience more risks during an intense magnetic storm than a strong one. The additional accumulated absorbed radiation doses and the excess SEU rates can reach 17% and 19%, respectively, relative to quiet conditions.
5. The previous results may formulate the reason of the failure of EGYPTSAT-2: The short-term activities occurring in the inner radiation belt and at the high latitudes were not included in the radiation analysis performed by Samwel and Hady (2009) who implemented the long-term averaged AP8 model. We showed that before the satellite was out of control, the solar activity was very intense, leading to the occurrence of a SEP event and several geomagnetic storms, hence creating convenient conditions for the solar protons to reach abundantly the high latitudinal regions and imposing excessive radiation risks on the satellite.

The particle simulations and the radiation analysis we have carried out in this paper aim to urge the space engineers to reconsider the selection of the electronic components and the shielding design of the future LEO space missions operating in the most intense part of the Van Allen belts. This would be achieved by considering a more realistic and dynamic inner radiation belt models during variable space weather conditions.

One of the future research directions suggested by Samwel and Hady (2009) was the assessment of the SEU rates for the previous EGYPTSAT-2 mission. We are delighted to accomplish this complementary work in a response of the Egyptian space program needs through presenting an adequate radiation analysis of the forthcoming space missions.

As future work, we plan to implement other particle types such as electrons and ions (i.e., helium) with different energy ranges, so that these various simulations would improve our understanding of the dynamic processes occurring in the radiation belts and their associated effects on spacecraft considering the space weather conditions.

Appendix A: Boris-Buneman Algorithm Implementation

According to Birdsall and Langdon (2004), the energy-conserving rotation in the momentum space in a time step h is defined by the phase angle:

$$t = \tan\frac{\theta}{2} = \frac{qB}{\gamma m}\frac{h}{2} \tag{A1}$$

And by using the half-angle formulas, we obtain that:

$$\tan\theta = \frac{2\tan\frac{\theta}{2}}{1-\tan^2\frac{\theta}{2}} = \frac{2t}{1-t^2} \tag{A2}$$

Therefore,

$$s = \sin\theta = \frac{2t}{1+t^2} \tag{A3}$$

And the complete $\mathbf{v}\times\mathbf{B}$ rotation becomes:

$$\mathbf{u}_* = \mathbf{u}_- + \mathbf{u}_- \times \mathbf{t} \tag{A4}$$

$$\mathbf{u}_+ = \mathbf{u}_- + \mathbf{u}_* \times \mathbf{s} \tag{A5}$$

Finally, the discretized form of the set of Equations 2 was implemented as follows:

$$\mathbf{u}_- = \mathbf{u}_{n-h/2} \tag{A6}$$

$$\mathbf{u}_* = \mathbf{u}_- + \mathbf{u}_- \times \mathbf{t} \tag{A7}$$

$$\mathbf{u}_+ = \mathbf{u}_- + \mathbf{u}_* \times \frac{2\mathbf{t}}{1+\mathbf{t}^2} \tag{A8}$$

$$\mathbf{u}_+ = \mathbf{u}_{n+h/2} \tag{A9}$$

$$\mathbf{r}_{n+\Delta t} = \mathbf{r}_n + \Delta t\frac{\mathbf{u}_+}{\gamma} \tag{A10}$$

where, $\mathbf{t} = \frac{qh}{2\gamma m}\mathbf{B}$.

Appendix B: SEU Calculation Procedure

The method developed by Bendel and Petersen (1983) estimated the upset rates in devices exposed to given proton fluxes within a particular spacecraft shielding using semi-empirical relations based on experimental works.

The procedure to compute the Single Event Upset (SEU) rates is described as follows:

1. Finding the experimental proton upset cross-sections at the energy range 70–180 MeV:
   The nuclear cross section of a nucleus is used to describe the probability that a nuclear reaction will occur. The concept of a nuclear cross section can be quantified physically in terms of "characteristic area" where a larger area means a larger probability of interaction. The experimental SEU cross sections were fitted to form a semi-empirical relation (Equation B1) which depends mainly on the device sensitivity "A" in MeV. We have selected the parameter A to be 18 which corresponds to the sensitivity of the static random-access memory (SRAM) 93425.

$$\sigma = (24/A)^{14}\left[1-\exp\left(-0.18Y^{0.5}\right)\right]^{4} \tag{B1}$$

   where,

$$Y = (18/A)^{0.5}[E-A] \tag{B2}$$

   where, σ is the fitted SEU cross sections in units of 10^{-12} upsets per proton/cm^2 per bit and Y is a linear function of energy in MeV (F. L. Petersen et al., 1982).

2. Finding the proton spectrum of the orbit considered:
   Through the output numerical results of the previous simulations, we selected a circular orbit to count from the geographical map the number of cells lying within different energy bins. The single cell represented a flux quantity which was defined by the number of protons passing through one unit area of 1 deg^2 (=1 degree of longitude × 1 degree of latitude) in 1 s. Next, a curve fit was applied to follow the general pattern of the proton spectrum at LEO orbit, as shown by Beck and Divita (1962) and Burrell (1964):

$$\phi_o(E) = HE^{-q};\ E_1 \le E \le E_2 \tag{B3}$$

   where, H and q are the curve fitting coefficients for a selected energy range from E_1 to E_2.

3. Selecting the shielding distribution for the devices in the spacecraft:
   For simplicity, we chose a single layer of Aluminum as shielding material with thickness 1 g/cm^2.

4. Obtaining the proton spectrum inside the shielding material:
   The corresponding differential energy spectrum formula at different depths in any material is,

$$\phi_X = \frac{HBE^{*(r-1)}}{\left(A+BE^{*r}\right)^{(r-q-1)/r}} \tag{B4}$$

   where,

$$E^{*} = \begin{cases} \left(\frac{E^{r}-A}{B}\right)^{1/r} & \text{if } E > A^{1/r} \\ 0 & \text{if } E < A^{1/r} \end{cases} \tag{B5}$$

   and,

$$A = \frac{1}{2b}(B-1) \tag{B6}$$

$$B = \exp\left(\frac{2bX}{a}\right) \tag{B7}$$

   knowing that ϕ_X and E^* are the proton flux and its energy inside the shielding material at the depth X respectively, and the coefficients a, b, and r are derived from empirical curves to determine the proton range in the given shielding material (Burrell, 1964).

5. Estimating the SEU rates by combining the proton upset cross-sections (step 1) with the proton spectrum (step 4).

Appendix C: Absorbed Radiation Dose Calculation Procedure

The absorbed radiation dose rate in material due to a primary charged particle beam was calculated by considering N number of particles with energy E entering a shielding material with density ρ and through a surface a during time Δt in a range of Δx and by assuming that each particle is responsible for the deposit of an energy $\Delta\epsilon$ (Antoni & Bourgois, 2017). Therefore, the general formulation of the absorbed dose in the irradiation area can be expressed as:

$$\bar{\dot{D}} = \frac{N\ \Delta\epsilon}{\rho\ a\ \Delta x\ \Delta t} \tag{C1}$$

If we reach the mass m to an infinitesimal amount at surface a and at depth Δx, the theoretical expression for absorbed dose rate is deduced as follows:

$$\dot{D} = \lim_{m\to 0}\frac{1}{\rho}\left(\frac{\Delta\epsilon}{\Delta x}\right)\left(\frac{N}{a\ \Delta t}\right) = \left(\frac{S}{\rho}\right)\dot{\Phi} \tag{C2}$$

where the $\dot{\Phi}$ (=flux) is the fluence rate and (S/ρ) is the mass stopping power.

Appendix D: Solar and Geomagnetic Activities

This appendix summarizes the geomagnetic (Figures D1 and D2) and solar (Figure D3) activities during March and April 2015.

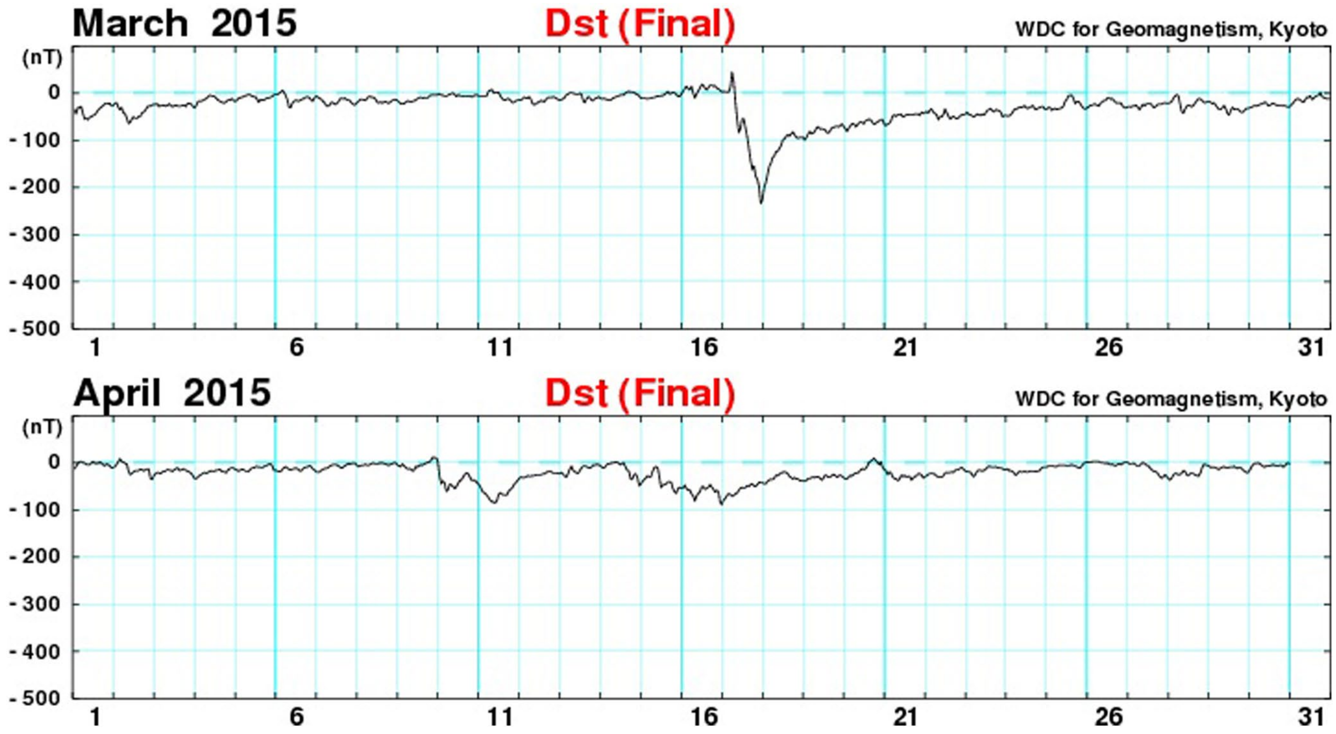

Figure D1. The *Dst* index profiles of March and April 2015.

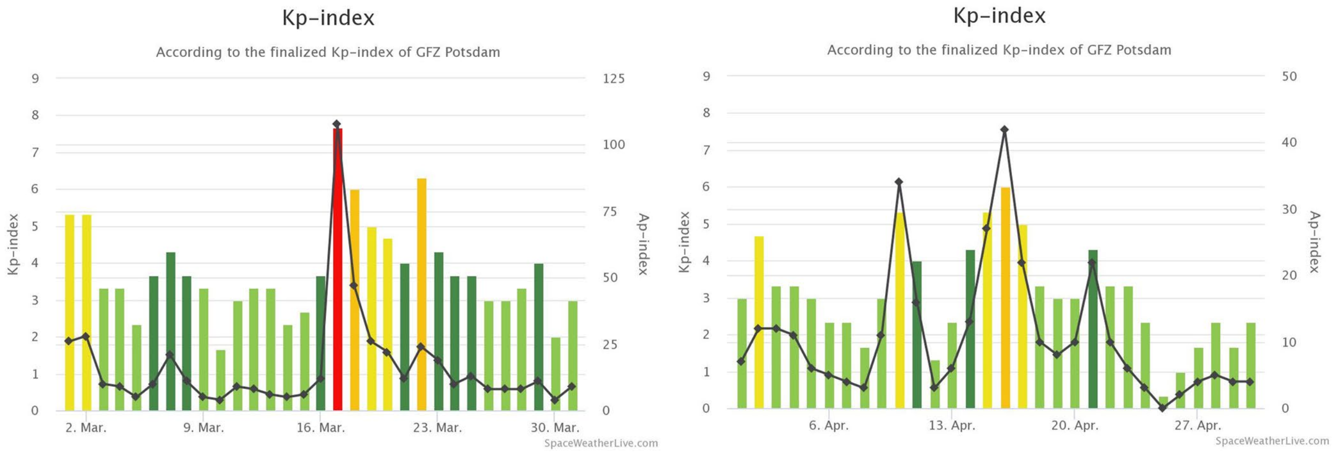

Figure D2. The geomagnetic activity reports of March and April 2015. The green bars correspond to Kp < 5, yellow bars to 5 < Kp < 7, and red bars to Kp > 7.

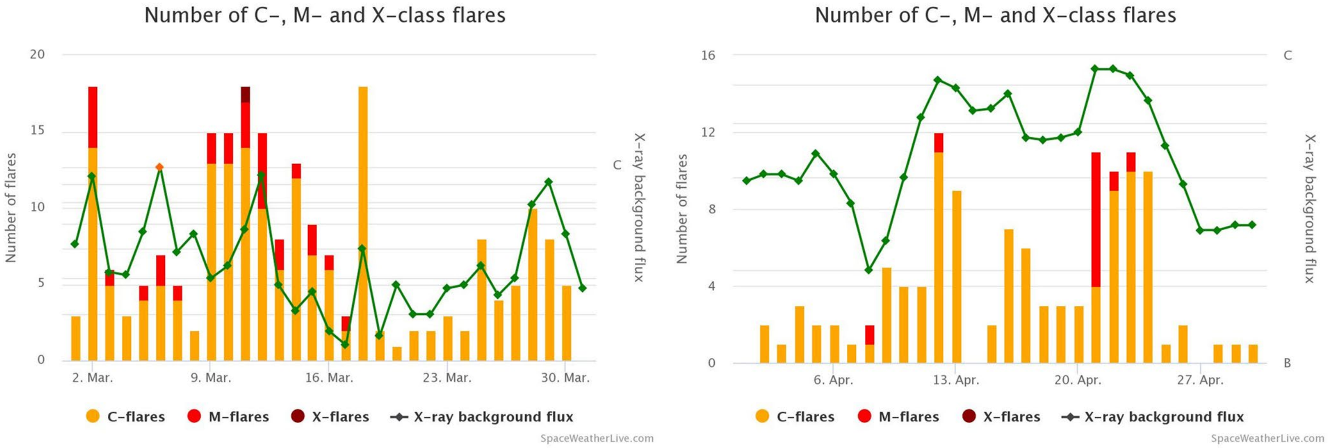

Figure D3. The flare activity history reports of March and April 2015.

Acronyms

HL	high-latitude
LL	low-latitude
PLEO	polar low-Earth orbit
NPLEO	near-polar low-Earth orbit

Data Availability Statement

The *Dst* index data was retrieved from World Data Center of Kyoto University: https://wdc.kugi.kyoto-u.ac.jp/dst_final/. The solar and geomagnetic reports were downloaded from the webpage of "SpaceWeatherLive": https://www.spaceweatherlive.com/en/archive/. The "Stopping Power and Range Tables for Protons" were provided from the National Institute of Standards and Technology (NIST): https://physics.nist.gov/PhysRefData/Star/Text/PSTAR.html. The SEP event list was supplied by the NOAA Space Environment Services Center: https://umbra.nascom.nasa.gov/SEP/. The mission status details of EGYPTSAT-2 are available on the ESA eoPortal: https://directory.eoportal.org/web/eoportal/satellite-missions/e/egyptsat-2#overview. The groundtrack codes are available in the textbook of Curtis (2014).

Acknowledgments

This work was supported by JSPS KAKENHI Grants: JP20H01961, JP21H04518, JP22K03707, and JP22K21345. Prof. Dr. Viviane Pierrard acknowledges the project 21GRD02 BIOSPHERE that has received funding from the European Partnership on Metrology, co-financed by the European Union's Horizon Europe Research and Innovation Programme and by the Participating States.

References

Ameri, D., & Valtonen, E. (2019). Potential role of energetic particle observations in geomagnetic storm forecasting. *Advances in Space Research*, *64*(3), 801–813. https://doi.org/10.1016/j.asr.2019.05.012

Antoni, R., & Bourgois, L. (2017). *Applied physics of external radiation exposure*. In (pp. 53–60). Springer International Publishing. https://doi.org/10.1007/978-3-319-48660-4

Beck, A. J., & Divita, E. L. (1962). Evaluation of space radiation doses received within a typical spacecraft. *American Rocket Society Journal*, *32*(11), 1668–1676. https://doi.org/10.2514/8.6360

Bendel, W. L., & Petersen, E. L. (1983). Proton upsets in orbit. *IEEE Transactions on Nuclear Science*, *30*(6), 4481–4485. https://doi.org/10.1109/TNS.1983.4333158

Birdsall, C., & Langdon, A. (2004). *Plasma physics via computer simulation*. In (pp. 58–59). Taylor & Francis. Retrieved from https://books.google.co.jp/books?id=S2lqgDTm6a4C

Blakely, E. A., Ngo, F. Q., Curtis, S. B., & Tobias, C. A. (1984). Heavy-ion radiobiology: Cellular studies. In *Advances in radiation biology* (p. 310). Elsevier. https://doi.org/10.1016/B978-0-12-035411-5.50013-7

Borthomieu, Y. (2014). Satellite lithium-ion batteries. In *Lithium-ion batteries* (pp. 311–344). Elsevier. https://doi.org/10.1016/B978-0-444-59513-3.00014-5

Burrell, M. O. (1964). *The calculation of proton penetration and dose rates (techreport No. NASA-TM-X-53063)*. NASA Marshall Space Flight Center Huntsville, . Retrieved from https://ntrs.nasa.gov/search.jsp?R=19640020596, https://ntrs.nasa.gov/archive/nasa/casi.ntrs.nasa.gov/19640020596.pdf

Curtis, H. D. (2014). *Orbital mechanics for engineering students* (3rd ed.). Butterworth-Heinemann. https://doi.org/10.1016/C2011-0-69685-1

Dachev, T. P. (2018). South-Atlantic anomaly magnetic storms effects as observed outside the international space station in 2008–2016. *Journal of Atmospheric and Solar-Terrestrial Physics*, *179*, 251–260. https://doi.org/10.1016/j.jastp.2018.08.009

Dachev, T. P., Bankov, N. G., Tomov, B. T., Matviichuk, Y. N., Dimitrov, P. G., Häder, D.-P., & Horneck, G. (2017). Overview of the ISS radiation environment observed during the ESA EXPOSE-r2 mission in 2014-2016. *Space Weather*, *15*(11), 1475–1489. https://doi.org/10.1002/2016sw001580

de Soria-Santacruz Pich, M., Jun, I., & Evans, R. (2017). Empirical radiation belt models: Comparison with in situ data and implications for environment definition. *Space Weather*, *15*(9), 1165–1176. https://doi.org/10.1002/2017SW001612

Engel, M. A., Kress, B. T., Hudson, M. K., & Selesnick, R. S. (2015). Simulations of inner radiation belt proton loss during geomagnetic storms. *Journal of Geophysical Research: Space Physics*, *120*(11), 9323–9333. https://doi.org/10.1002/2015ja021568

Falguere, D., Boscher, D., Nuns, T., Duzellier, S., Bourdarie, S., Ecoffet, R., et al. (2002). In-flight observations of the radiation environment and its effects on devices in the SAC-C polar orbit. *IEEE Transactions on Nuclear Science*, *49*(6), 2782–2787. https://doi.org/10.1109/TNS.2002.805380

Girgis, K., Hada, T., Matsukiyo, S., Yoshikawa, A., Lemaire, J., Pierrard, V., & Samwel, S. (2022). *Proton flux modeling due to solar proton injections during geomagnetic storms* (Vol. SM44C-06). American Geophysical Union (AGU). Retrieved from 2022AGUFMSM44C..06G

Girgis, K. M., & Hada, T. (2018). Long-term variations of the solar wind effects on South Atlantic Anomaly (SAA) using Tsyganenko model. In *International exchange and innovation conference on engineering & sciences (IEICES)* (Vol. 4, pp. 36–41). Kyushu University. https://doi.org/10.15017/1960662

Girgis, K. M., Hada, T., & Matsukiyo, S. (2020a). Solar wind parameter and seasonal variation effects on the South Atlantic anomaly using Tsyganenko Models. *Earth Planets and Space*, *72*(100), 1–17. https://doi.org/10.1186/s40623-020-01221-2

Girgis, K. M., Hada, T., & Matsukiyo, S. (2020b). Space weather effects on proton flux variations in the South Atlantic anomaly: A numerical study performed by test particle simulations. In *European geosciences union (EGU) general assembly 2020*. https://doi.org/10.5194/egusphere-egu2020-1551

Girgis, K. M., Hada, T., & Matsukiyo, S. (2021). Estimation of single event upset (SEU) rates inside the SAA during the geomagnetic storm event of 15 May 2005. In *2021 ieee international conference on wireless for space and extreme environments (WiSEE)* (pp. 27–30). IEEE. https://doi.org/10.1109/WiSEE50203.2021.9613828

Girgis, K. M., Hada, T., & Matsukiyo, S. (2022). Seasonal variation and geomagnetic storm index effects on the proton flux response in the South Atlantic Anomaly by test particle simulations. *Journal of Atmospheric and Solar-Terrestrial Physics*, *228*(105808), 1–9. https://doi.org/10.1016/j.jastp.2021.105808

Girgis, K. M., Hada, T., Matsukiyo, S., & Yoshikawa, A. (2021). Inner radiation belt simulations of the proton flux response in the South Atlantic anomaly during the geomagnetic storm of 15 May 2005. *Journal of Space Weather and Space Climate*, *11*(48), 1–10. https://doi.org/10.1051/swsc/2021031

Girgis, K. M., Hada, T., Matsukiyo, S., & Yoshikawa, A. (2022). Radiation analysis of LEO mission in the South Atlantic anomaly during geomagnetic storm. *IEEE Journal of Radio Frequency Identification*, *6*, 292–298. https://doi.org/10.1109/JRFID.2022.3163441

Goldstein, J., Angelopoulos, V., Pascuale, S. D., Funsten, H. O., Kurth, W. S., Llera, K., et al. (2017). Cross-scale observations of the 2015 St. Patrick's Day storm: THEMIS, Van Allen Probes, and TWINS. *Journal of Geophysical Research: Space Physics*, *122*(1), 368–392. https://doi.org/10.1002/2016JA023173

Hudson, M. K., Elkington, S. R., Lyon, J. G., Marchenko, V. A., Roth, I., Temerin, M., et al. (1997). Simulations of radiation belt formation during storm sudden commencements. *Journal of Geophysical Research*, *102*(A7), 14087–14102. https://doi.org/10.1029/97ja03995

Kress, B. T., Hudson, M. K., & Slocum, P. L. (2005). Impulsive solar energetic ion trapping in the magnetosphere during geomagnetic storms. *Geophysical Research Letters*, *32*(6), L06108. https://doi.org/10.1029/2005gl022373

Kress, B. T., Mertens, C. J., & Wiltberger, M. (2010). Solar energetic particle cutoff variations during the 29–31 October 2003 geomagnetic storm. *Space Weather*, *8*(5). https://doi.org/10.1029/2009sw000488

Lemaire, J., Batteux, S., & Slypen, I. (2005). The influence of a southward and northward turning of the interplanetary magnetic field on the geomagnetic cut-off of cosmic rays, on the mirror points positions of geomagnetically trapped particles, and on their rate of precipitations in the atmosphere. *Journal of Atmospheric and Solar-Terrestrial Physics*, *67*(7), 719–727. https://doi.org/10.1016/j.jastp.2004.09.008

Leske, R. A., Mewaldt, R. A., Stone, E. C., & von Rosenvinge, T. T. (2001). Observations of geomagnetic cutoff variations during solar energetic particle events and implications for the radiation environment at the space station. *Journal of Geophysical Research*, *106*(A12), 30011–30022. https://doi.org/10.1029/2000JA000212

Mao, H.-S., & Wirz, R. (2011). Comparison of charged particle tracking methods for non-uniform magnetic fields. In *42nd AIAA plasmadynamics and lasers conference*. American Institute of Aeronautics and Astronautics. https://doi.org/10.2514/6.2011-3739

Mertens, C. J., Kress, B. T., Wiltberger, M., Blattnig, S. R., Slaba, T. S., Solomon, S. C., & Engel, M. (2010). Geomagnetic influence on aircraft radiation exposure during a solar energetic particle event in October 2003. *Space Weather*, *8*(3). https://doi.org/10.1029/2009sw000487

National Research Council. (2000). *Radiation and the international space station: Recommendations to reduce risks*. The National Academies Press. https://doi.org/10.17226/9725

Petersen, E. (2011). *Single event effects in aerospace*. John Wiley & Sons.

Petersen, F. L., Shapiro, P., Adams, J. H., & Burke, E. A. (1982). Calculation of cosmic-ray induced soft upsets and scaling in VLSI devices. *IEEE Transactions on Nuclear Science*, *29*(6), 2055–2063. https://doi.org/10.1109/TNS.1982.4336495

Pierrard, V., Benck, S., Botek, E., Borisov, S., & Winant, A. (2023). Proton flux variations during solar energetic particle events, minimum and maximum solar activity, and splitting of the proton belt in the South Atlantic anomaly. *Journal of Geophysical Research: Space Physics*, *128*(5), e2022JA031202. https://doi.org/10.1029/2022ja031202

Pierrard, V., Lopez Rosson, G., Borremans, K., Lemaire, J., Maes, J., Bonnewijn, S., et al. (2014). The energetic particle telescope: First results. *Space Science Reviews*, *184*(1–4), 87–106. https://doi.org/10.1007/s11214-014-0097-8

Pierrard, V., & Rosson, G. L. (2016). The effects of the big storm events in the first half of 2015 on the radiation belts observed by EPT/PROBA-v. *Annales Geophysicae*, *34*(1), 75–84. https://doi.org/10.5194/angeo-34-75-2016

Qin, M., Zhang, X., Ni, B., Song, H., Zou, H., & Sun, Y. (2014). Solar cycle variations of trapped proton flux in the inner radiation belt. *Journal of Geophysical Research: Space Physics*, *119*(12), 9658–9669. https://doi.org/10.1002/2014JA020300

Saito, S., Miyoshi, Y., & Seki, K. (2010). A split in the outer radiation belt by magnetopause shadowing: Test particle simulations. *Journal of Geophysical Research*, *115*(A8). https://doi.org/10.1029/2009JA014738

Samwel, S. W., & Hady, A. A. (2009). Space radiation environment forecast for EGYPTSAT-2 satellite. *Space Weather*, *7*(12), S12004. https://doi.org/10.1029/2009SW000482

Selesnick, R. S., Hudson, M. K., & Kress, B. T. (2010). Injection and loss of inner radiation belt protons during solar proton events and magnetic storms. *Journal of Geophysical Research*, *115*(A8), A08211. https://doi.org/10.1029/2010JA015247

Shreedevi, P. R., Choudhary, R. K., Thampi, S. V., Yadav, S., Pant, T. K., Yu, Y., et al. (2020). Geomagnetic storm-induced plasma density enhancements in the southern polar ionospheric region: A comparative study using St. Patrick's Day storms of 2013 and 2015. *Space Weather*, *18*(8). https://doi.org/10.1029/2019SW002383

Slocum, P. L., Blake, J. B., Fennell, J. F., Hudson, M. K., Looper, M. D., Lorentzen, K. R., & Mazur, J. E. (2002). Observations of ion injections during large solar energetic particle events. In *AGU fall meeting abstracts* (Vol. 2002). SM51A-0501.

Smart, D. F., & Shea, M. A. (1994). Geomagnetic cutoffs: A review for space dosimetry applications. *Advances in Space Research*, *14*(10), 1994–2796. https://doi.org/10.1016/0273-1177(94)90543-6

Smart, D. F., & Shea, M. A. (2005). A review of geomagnetic cutoff rigidities for Earth-orbiting spacecraft. *Advances in Space Research*, *36*(10), 2012–2020. https://doi.org/10.1016/j.asr.2004.09.015

Suess, S. T. & Tsurutani, B. T. (Eds.) (1998). *From the Sun: Auroras, magnetic storms, solar flares, cosmic rays*. American Geophysical Union. https://doi.org/10.1029/SP050

Thébault, E., C Finlay, C., D Beggan, C., Alken, P., Aubert, J., Barrois, O., et al. (2015). International geomagnetic reference field: The 12th generation. *Earth Planets and Space*, *67*(1), 79. https://doi.org/10.1186/s40623-015-0228-9

Tsyganenko, N. A. (2002). A model of the near magnetosphere with a dawn-dusk asymmetry 1. Mathematical structure. *Journal of Geophysical Research*, *107*(A8), SMP12-1–SMP12-15. https://doi.org/10.1029/2001JA000219

Tsyganenko, N. A., & Sitnov, M. I. (2005). Modeling the dynamics of the inner magnetosphere during strong geomagnetic storms. *Journal of Geophysical Research*, *110*(A3), A03208. https://doi.org/10.1029/2004JA010798

Venkatesh, K., Ram, S. T., Fagundes, P. R., Seemala, G. K., & Batista, I. S. (2017). Electrodynamic disturbances in the Brazilian equatorial and low-latitude ionosphere on St. Patrick's Day storm of 17 march 2015. *Journal of Geophysical Research: Space Physics*, *122*(4), 4553–4570. https://doi.org/10.1002/2017JA024009

Wilson, J. (1978). Environmental geophysics and SPS shielding (lbl–8581). In S. B. Schimmerling, & W. Curtis (Eds.), *Workshop on the radiation environment of the satellite power system* (Vol. 11, pp. 33–116). Lawrence Berkeley National Laboratory. Retrieved from https://escholarship.org/uc/item/6d45z9dz

Wu, C.-C., Liou, K., Lepping, R. P., Hutting, L., Plunkett, S., Howard, R. A., & Socker, D. (2016). The first super geomagnetic storm of solar cycle 24: "The St. Patrick's Day event (17 March 2015)". *Earth Planets and Space*, *68*(1), 151. https://doi.org/10.1186/s40623-016-0525-y

Xapsos, M., Barth, J., Stassinopoulos, E., Messenger, S., Walters, R., Summers, G., & Burke, E. (2000). Characterizing solar proton energy spectra for radiation effects applications. *IEEE Transactions on Nuclear Science*, *47*(6), 2218–2223. https://doi.org/10.1109/23.903756

Xapsos, M., Summers, G., Barth, J., Stassinopoulos, E., & Burke, E. (1999). Probability model for worst case solar proton event fluences. *IEEE Transactions on Nuclear Science*, *46*(6), 1481–1485. https://doi.org/10.1109/23.819111

Xu, Z., Hartinger, M. D., Clauer, C. R., Peek, T., & Behlke, R. (2017). A comparison of the ground magnetic responses during the 2013 and 2015 St. Patrick's Day geomagnetic storms. *Journal of Geophysical Research: Space Physics*, *122*(4), 4023–4036. https://doi.org/10.1002/2016JA023338

Zou, H., Li, C., Zong, Q., Parks, G. K., Pu, Z., Chen, H., et al. (2015). Short-term variations of the inner radiation belt in the South Atlantic Anomaly. *Journal of Geophysical Research: Space Physics*, *120*(6), 4475–4486. https://doi.org/10.1002/2015JA021312

Zou, H., Zong, Q. G., Parks, G. K., Pu, Z. Y., Chen, H. F., & Xie, L. (2011). Response of high-energy protons of the inner radiation belt to large magnetic storms. *Journal of Geophysical Research*, *116*(A10), A10229. https://doi.org/10.1029/2011JA016733